Publication Year	2020
Acceptance in OA	2025-03-10T10:52:24Z
Title	Different Fates of Young Star Clusters after Gas Expulsion
Authors	Pang, Xiaoying, Li, Yuqian, Tang, Shih-Yun, PASQUATO, Mario, Kouwenhoven, M. B. N.
Publisher's version (DOI)	10.3847/2041-8213/abad28
Handle	http://hdl.handle.net/20.500.12386/36577
Journal	THE ASTROPHYSICAL JOURNAL LETTERS
Volume	900

The Astrophysical Journal Letters, 900:L4 (10pp), 2020 September 1 https://doi.org/10.3847/2041-8213/abad28

Different Fates of Young Star Clusters after Gas Expulsion

Xiaoying Pang[1,2], Yuqian Li[1], Shih-Yun Tang[3,4], Mario Pasquato[5,6], and M. B. N. Kouwenhoven[1]

[1] Department of Physics, Xi'an Jiaotong-Liverpool University, 111 Ren'ai Road, Dushu Lake Science and Education Innovation District, Suzhou 215123, Jiangsu Province, People's Republic of China; Xiaoying.Pang@xjtlu.edu.cn

[2] Shanghai Key Laboratory for Astrophysics, Shanghai Normal University, 100 Guilin Road, Shanghai 200234, People's Republic of China

[3] Lowell Observatory, 1400 West Mars Hill Road, Flagstaff, AZ 86001, USA

[4] Department of Astronomy and Planetary Sciences, Northern Arizona University, Flagstaff, AZ 86011, USA

[5] INAF–Osservatorio Astronomico di Padova, Vicolo dell'Osservatorio 5, I-35122 Padova, Italy

[6] INFN–Sezione di Padova, Via Marzolo 8, I-35131 Padova, Italy

Received 2020 June 29; revised 2020 August 4; accepted 2020 August 5; published 2020 August 25

Abstract

We identify structures of the young star cluster NGC 2232 in the solar neighborhood (323.0 pc) and a newly discovered star cluster, LP 2439 (289.1 pc). Member candidates are identified using the Gaia DR2 sky position, parallax, and proper-motion data by an unsupervised machine-learning method, StarGO. Member contamination from the Galactic disk is further removed using the color–magnitude diagram. The four identified groups (NGC 2232, LP 2439, and two filamentary structures) of stars are coeval with an age of 25 Myr and were likely formed in the same giant molecular cloud. We correct the distance asymmetry from the parallax error with a Bayesian method. The 3D morphology shows the two spherical distributions of clusters NGC 2232 and LP 2439. Two filamentary structures are spatially and kinematically connected to NGC 2232. Both NGC 2232 and LP 2439 are expanding. The expansion is more significant in LP 2439, generating a loose spatial distribution with shallow volume number and mass density profiles. The expansion is suggested to be mainly driven by gas expulsion. With 73% of the cluster mass bound, NGC 2232 is currently experiencing a process of revirialization, However, LP 2439, with 52% of the cluster mass unbound, may fully dissolve in the near future. The different survivability traces the different dynamical states of NGC 2232 and LP 2439 prior to the onset of gas expulsion. While NGC 2232 may have been substructured and subvirial, LP 2439 may have either been virial/supervirial or experienced a much faster rate of gas removal.

Unified Astronomy Thesaurus concepts: Star clusters (1567); Open star clusters (1160)

1. Introduction

Star clusters form from dense gas clumps inside giant molecular clouds (GMCs). Only a fraction of the gas in a GMC is converted into stars, while the remainder of the gas is expelled from the cluster-forming clumps at later times. Therefore, the dynamics of star clusters embedded in the molecular cloud is dominated by the gravitational potential of the gas from which star clusters are formed (Lada & Lada 2003). Feedback from high-mass stars such as supernovae, stellar winds, and radiation will remove the intracluster gas within several million yr, which rapidly reduces the gravitational potential of the star cluster. This results in a star cluster expansion over a period of 4–10 Myr from an initial radius of 1–2 pc, depending on how rapidly the gas is removed (see Kroupa 2005; Baumgardt & Kroupa 2007). Most star clusters will lose a significant fraction of their stellar mass after the phase gas dispersal and often completely dissolve into the galactic field. This is usually referred to as infant mortality (de Grijs & Goodwin 2008). In recent years, many studies investigated the processes and effects of gas dispersal on the evolution of young clusters (e.g., Hills 1980; Goodwin & Bastian 2006; Baumgardt & Kroupa 2007; Banerjee & Kroupa 2013; Brinkmann et al. 2017; Shukirgaliyev et al. 2017; Farias et al. 2018; Dinnbier & Kroupa 2020a, 2020b, and references therein).

The dynamical state of the star cluster at the onset of gas expulsion plays a crucial role in determining the survival chances of a star cluster after the gas has been removed. If the gas expulsion occurs when the cluster is dynamically subvirial and has a substructured spatial distribution, the survival rate of the cluster is considerably higher (Goodwin 2009; Farias et al. 2015, 2018). Moreover, the faster the gas is expelled from the cluster, the lower the bound fraction of mass for the remaining cluster members is (Brinkmann et al. 2017). If the stellar mass of a protocluster is more centrally concentrated than that of the gas, as obtained in the cluster formation model of Parmentier & Pfalzner (2013), the survival rate of star clusters is also much higher (Adams 2000; Shukirgaliyev et al. 2017).

The young star clusters that emerge from their parental molecular clouds shortly after gas expulsion will enter a phase of violent relaxation, which is the phase in which the star clusters evolve from a nonequilibrium state toward a new state of equilibrium (Lynden-Bell 1967). If the cluster succeeds in obtaining virial equilibrium during this phase, it is said to have been revirialized. Several young massive clusters, such as R136, Westerlund 1, and Cep OB3b, manage to regain virialization within a time shorter than their present age (Cottaar et al. 2012; Banerjee & Kroupa 2013; Karnath et al. 2019). On the other hand, the revirialization time is substantially longer than the age of several other young clusters, for example, in the cases of IC 2602, IC 2391, and NGC 2547 (Bravi et al. 2018). These clusters are supervirial and continue to expand. Even some open clusters may manage to revirialize, the Galactic tides continue to promote expansion among open clusters above 1 Gyr (Pang et al. 2018).

In addition to gas expulsion, the two-body relaxation process in a cluster can also trigger expansion of the cluster. However, the expansion rate induced by two-body relaxation is substantially smaller than that resulting from gas expulsion (see, e.g., Kroupa 2005; Moeckel et al. 2012; Dinnbier & Kroupa 2020a, 2020b). Simultaneously, mass segregation occurs as a by-product of two-body relaxation, as the cluster members attempt to achieve a state of energy equipartition (e.g., Pang et al. 2013). Thus far, no astrometric efforts have been made to distinguish these two drivers of expansion in star clusters. Testing these scenarios using observations of young star clusters shortly after gas expulsion has occurred is crucial to understand the disruption process of star clusters.

The young open cluster NGC 2232 has an age of 25–29 Myr (Currie et al. 2008; Liu & Pang 2019) and is located south of the Galactic plane at the position of R.A. $= 96\overset{\circ}{.}9973$, decl. $= -04\overset{\circ}{.}7929$ (Gaia Collaboration et al. 2018b). Unlike its neighbor, the Orion star-forming complex, NGC 2232 has not attracted much attention. There exist only a few comprehensive studies of this cluster. Claria (1972) carried out the first *UBV*-photometry study of this cluster and estimated its age to be 20 Myr. They measured the interstellar reddening of the cluster as $E(B-V) = 0.01$ mag and obtained a distance of 360 pc. The latter measurement of the reddening was refined to 0.06 ± 0.03 mag in the first spectroscopic study of 16 cluster members by Levato & Malaroda (1974). Lyra et al. (2006) constrained the reddening in the color–color diagram by studying eight evolved B-type stars, which gave a best-fit reddening of $E(B-V) = 0.07 \pm 0.02$ mag.

Young star clusters that are still partially embedded in the gas and dust of their parental molecular clouds tend to have a high interstellar reddening. This phenomenon is seen in the Orion Nebula Cluster, which has differential reddening of several orders of magnitude (Scandariato et al. 2011). Also, the reddening of the 1 Myr old cluster NGC 3603 can reach 1.5 mag (Pang et al. 2011). The low reddening of NGC 2232 thus indicates that it probably has already undergone gas expulsion.

Located right next to NGC 2232 (within 50 pc) is a newly discovered star cluster, LP 2439, that was recently found by Liu & Pang (2019; ID: 2439). This star cluster has not appeared in any study since its discovery in 2019. According to Liu & Pang (2019), LP 2439 has an age similar to that of NGC 2232. Note that a common age does not necessarily imply a similar dynamical evolutionary stage, as the dynamical ages of star clusters may be quantified using the number of crossing times since their formation (see Section 5). We therefore select both clusters as targets to investigate the expansion and dynamical state of star clusters after gas expulsion.

Using the data from the Gaia second data release (DR2), we explore the neighborhood of NGC 2232 and LP 2439 and investigate their dynamical state after gas expulsion. In Section 2, we discuss the quality and limitations of the Gaia DR2 data and describe our input data set for structure identification. We then present the algorithm, StarGO, which is used to identify structures. Further confirmation of membership is performed using the color–magnitude diagram (CMD). The properties of the identified member candidates are presented and discussed in Section 3, including the discussion of the evidence of gas expulsion. The 3D morphology of NGC 2232, LP 2439, and the nearby associated structures is discussed in Section 4 along with our interpretation of the results. The fate and dynamical state of both clusters are discussed in Section 5. Finally, we provide a brief summary in Section 6.

2. Data Analysis and Member Determination

2.1. Gaia DR2 Data Processing and Analysis

The DR2 of Gaia (Gaia Collaboration et al. 2018a) has provided more than 1 billion sources with parallaxes (ϖ) and proper motions (PMs; $\mu_\alpha \cos\delta$, μ_δ) with unprecedented precision and sensitivity. The *G*-band (330–1050 nm) photometry ranges from ~3 to 21 mag. The median uncertainty of ϖ ranges from ~0.04 mas for bright sources ($G < 14$ mag) to ~0.7 mas for faint ones ($G \approx 20$ mag). The corresponding uncertainties of the PMs for these sources are 0.05 and 1.2 mas yr^{-1}, respectively (Lindegren et al. 2018). Only 7.2 million stars have radial velocity (RV) measurements in the Gaia DR2 (Cropper et al. 2018) with a typical uncertainty of 2 km s^{-1}.

The spatial and kinematic structures of NGC 2232 and its neighboring cluster, LP 2439, are investigated using Gaia DR2 data within 100 pc of the center of NGC 2232. In Cartesian galactocentric coordinates, the center of NGC 2232 is located at $(X, Y, Z) = (-8566.0, -183.1, -14.0)$ pc.[7] The distance to NGC 2232 is taken to be 325.6 pc (Gaia Collaboration et al. 2018b), and the equatorial coordinates of its center are R.A. $= 96\overset{\circ}{.}9973$, decl. $= -04\overset{\circ}{.}7929$ (J2000; from Gaia Collaboration et al. 2018b).

We apply the same astrometric quality cuts as Lindegren et al. (2018, their Appendix C) to exclude possible artifacts in the Gaia DR2 from our sample. The final "cleaned" sample contains 131,066 sources. Hereafter, we refer to this set as "sample I." The stars in sample I have *G* magnitudes ranging between ~4.2 and ~19.5 mag, and the sample becomes significantly incomplete for $G \gtrsim 19$ mag.

Figure 1(a) shows a 2D density map of PMs that only shows bins with overdensities $>3\sigma$ in sample I. Several overdensities stand out. There is an overdensity near the average PMs of NGC 2232 (indicated with a blue plus sign, $(\mu_\alpha \cos\delta, \mu_\delta) = (-4.734, -1.844)$ mas yr^{-1}; Liu & Pang 2019). Another overdensity is seen at $(\mu_\alpha \cos\delta, \mu_\delta) = (-7.381, -2.569)$ mas yr^{-1} (red plus sign; Liu & Pang 2019). This group corresponds to LP 2439. The notable clustering at $\mu_\alpha \cos\delta < 0$ and $\mu_\delta < 0$ mas yr^{-1} is the Orion star-forming complex (Jerabkova et al. 2019). An isolated overdensity around $(\mu_\alpha \cos\delta, \mu_\delta) = (-5.310, 5.014)$ mas yr^{-1} relates to another new star cluster discovered by Liu & Pang (2019; ID: 2383), which is located at a distance of 377 pc (Liu & Pang 2019) and does not show any spatial connection to NGC 2232. We apply a circular cut with a radius of 2.8 mas yr^{-1} (black circle in Figure 1(a)) to only include NGC 2232 and LP 2439 for further analysis. This reduces the number of stars to 5843; we refer to this set of stars as "sample II" hereafter. The stars in this sample have magnitudes ranging between $G \sim 5.2$ and ~19.3 mag, and the sample is complete for $G \lesssim 18.0$ mag. Note that the stars in sample II are typically fainter than the stars in sample I, since the brightest stars, which reside in the Orion star-forming complex, have been removed.

---

[7] The Cartesian Galactic coordinate system adopted in our study is defined as follows. The Galactic center ($l = 0°$ and $b = 0°$) is located at the origin of the coordinate system. The positive *X*-axis points from the projection of the Sun's position onto the Galactic midplane toward the Galactic center. The positive *Y*-axis points toward $l = 90°$, and the positive *Z*-axis points toward $b = 90°$. Further details about the coordinate system can be found in the Appendix of Tang et al. (2019).

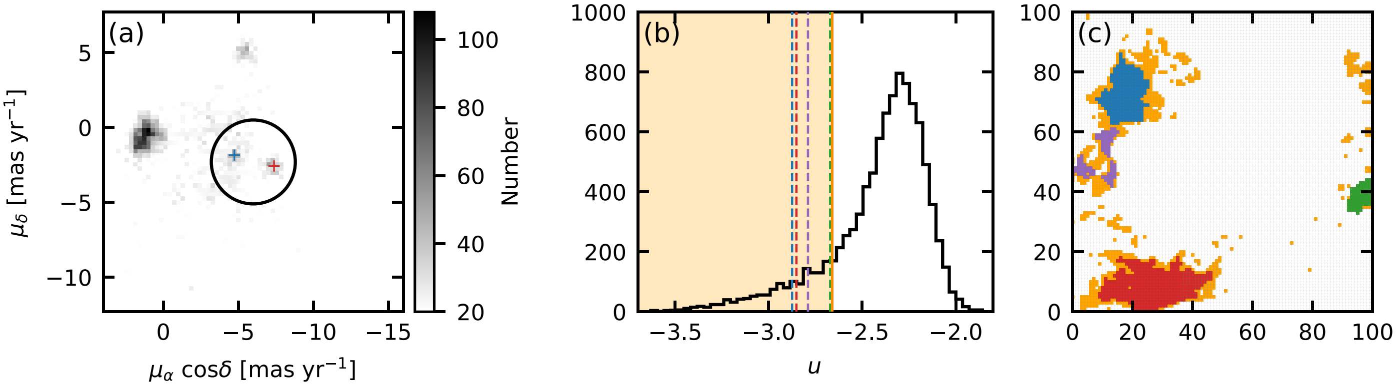

Figure 1. (a) The 2D density map of the PM vectors for the regions around NGC 2232 and LP 2439 in sample I. The blue and red plus signs indicate the overdensities generated by NGC 2232 and LP 2439, respectively. Each bin is smoothed by the neighboring eight bins, and here only bins with a number count $>3\sigma$ are shown, where σ is the standard deviation of all bins. The color bar indicates the number count in each bin. (b) Histogram of the distribution of u. The orange solid line shows the position $u_{\rm peak-3\sigma}$. The left tail with $u < u_{\rm peak-3\sigma}$ is highlighted in orange, corresponding to the orange patches in panel (c). The blue, red, purple, and green dashed lines denote the threshold values of u. Values smaller than this threshold produce the 5% contamination rate among identified candidates for the red, blue, purple, and green patches in SOM (panel (c)). (c) The 2D 100 × 100 neural map resulting from SOM. The neurons with u smaller than the threshold values (blue, red, purple, and green dashed lines in panel (b)) of the 5% contamination rate are shown in blue, red, purple, and green. The two dominant neuron groups are traced with blue (NGC 2232) and red (LP 2439).

In this study, we use the 5D parameters of stars in sample II (R.A., decl., ϖ, $\mu_\alpha \cos\delta$, and μ_δ) from Gaia DR2. Since only a fraction of the stars (∼12%) have RV measurements, RV measurements are used as supplementary data. Adopting a distance of $1/\varpi$, we compute for each source the galactocentric Cartesian coordinates (X, Y, Z). The transformation is performed by using the Python `Astropy` package (Astropy Collaboration et al. 2013, 2018). Considering the asymmetric error in the distance that arises from the direct inversion of ϖ, a Bayesian method is adopted to correct individual distances of stars in Section 4.

2.2. *Member Identification*

The unsupervised machine-learning method, StarGO (Yuan et al. 2018),[8] is used for member candidate selection. This algorithm is based on the self-organizing map (SOM) method that maps high-dimension data down to two dimensions while preserving the topological structures of the data. StarGO has been successfully used in the identification of tidal structures in open clusters, such as the Coma Berenices cluster (Tang et al. 2019) and Blanco 1 (Zhang et al. 2020).

We apply StarGO to map a 5D data set (X, Y, Z, $\mu_\alpha \cos\delta$, μ_δ) of the clusters NGC 2232 and LP 2439 and their surrounding region (sample II) onto a 2D neural network to identify member candidates. We adopt a network with 100 × 100 neurons represented by the 100 × 100 grid elements in Figure 1(c) to study sample II. Each neuron is assigned a random 5D weight vector that has the same dimensions as the input 5D parameters (X, Y, Z, $\mu_\alpha \cos\delta$, μ_δ) obtained from observations. The weight vector of each neuron is updated during each iteration so that it is closer to the input vector of an observed star. This learning process is iterated 400 times, until the weight vectors converge. The value of the difference of the weight vectors between adjacent neurons, u, is small when the 5D weight vectors of the adjacent neurons are similar, indicating that stars associated with neurons are spatially and kinematically coherent. The neurons with small values of u will group together in the 2D SOM map as patches (see Figure 1(c)). Different patches correspond to different groupings of stars. Neurons located inside the patch have smaller u values than neurons outside it. Therefore, u values of neurons inside patches generate an extended tail on the left (toward the small value) in the u histogram (see Figure 1(b)).

A cut on the tail of the u distribution is used for member selection. Tang et al. (2019) and Zhang et al. (2020) selected member candidates in the extended tail of the u distribution, with u values less than the value of the peak $u_{\rm peak}$ minus the 99.85th percentile $\Delta_{3\sigma}$ ($u \leqslant u_{\rm peak} - \Delta_{3\sigma}$; see their Figure 3). Note that our samples cover the Galactic midplane. Therefore, contamination by field stars with similar PMs to those of cluster members is much higher than for Coma Berenices (Tang et al. 2019) and Blanco 1 (Jackson et al. 2020; Zhang et al. 2020), which are 100–200 pc off the midplane. Applying the u-cut criteria, $u \leqslant u_{\rm peak} - \Delta_{3\sigma}$ (orange vertical line in Figure 1(b)) results in a 13.3% field star contamination rate in selected patches that showed up in the SOM (orange patches in Figure 1(c)), which is double the value of ∼5%–6% in Coma Berenices (Tang et al. 2019) and Blanco 1 (Zhang et al. 2020).

The contamination rate is evaluated from the smooth Galactic disk population using the Gaia DR2 mock catalog (Rybizki et al. 2018) by applying the same PM cut as described in Section 2.1 to the mock catalog in the same volume of the sky. Each of these mock stars is attached to the trained SOM map, from which we can compute the number of field stars associated with selected patches.

In order to reduce field star contamination, the selection of u is chosen to ensure a similar contamination rate of ∼5% for the different selected patches (blue, red, purple, and green dashed lines in Figure 1(b)). We show the two major clusters, NGC 2232 and LP 2439, in blue and red, respectively. The two additional smaller groups are shown in purple and green. Three small purple patches merge into NGC 2232 as one big group (orange patches) if we apply a u cut of $u_{\rm peak} - \Delta_{3\sigma}$. Considering their similarity, the purple patches are considered as a single group. The properties of NGC 2232, LP 2439, and the neighboring groups will be discussed further in Section 3. In the end, we have 182 member candidates for NGC 2232 (blue), 331 for LP 2439 (red), 79 for the purple group, and 61 for the green group.

---

[8] https://github.com/salamander14/StarGO

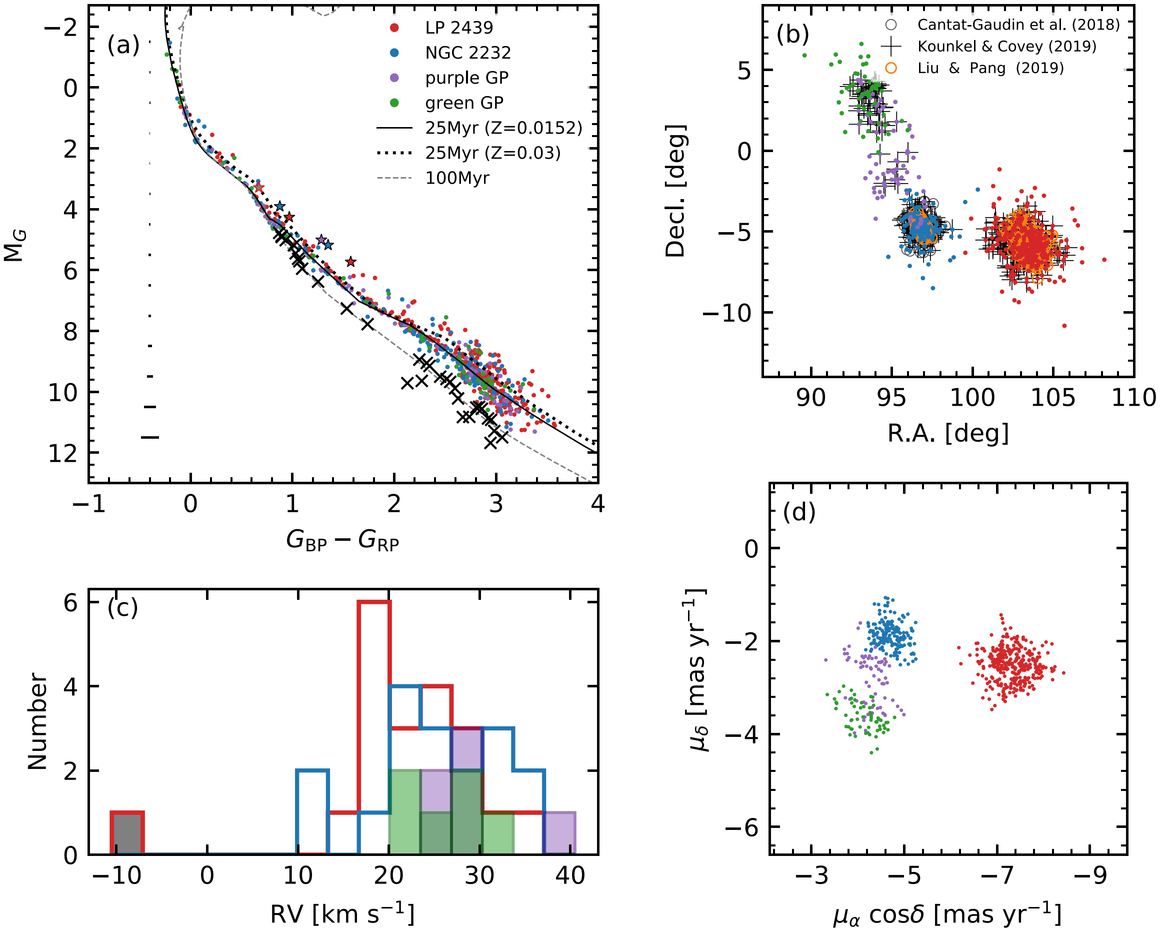

Figure 2. General properties of identified member candidates. (a) The CMD of the Gaia DR2 absolute magnitude M_G (adopting the Gaia DR2 parallax) for candidate stars identified by StarGO. Red and blue dots are candidate members of LP 2439 and NGC 2232. Purple and green dots indicate candidates of the purple and green groups in Figure 1(c). Crosses indicate field contaminants that are excluded from further investigation. The PARSEC isochrones of 25 and 100 Myr are overplotted as the black solid curve and gray dashed curve, with $E(B-V) = 0.07$ mag (Lyra et al. 2006) corrected and solar metallicity assumed. The black dotted curve is the PARSEC isochrone of 25 Myr adopting the same reddening but a supersolar metallicity of [Fe/H] = 0.32 (Monroe & Pilachowski 2010). The stars indicate binary candidates. The red outlined gray shaded star corresponds to the gray shaded bin in panel (c). The uncertainties of the colors are indicated with horizontal error bars. The typical G-magnitude error is 0.002 mag. (b) Spatial distribution of member candidates after CMD cleaning. The symbols and colors of the member candidates are the same as those in panel (a). Members are crossmatched with previous catalogs: Cantat-Gaudin et al. (2018), black open circles; Kounkel & Covey (2019), black plus signs; and Liu & Pang (2019), orange open circles. (c) The RV histograms for LP 2439 (red), NGC 2232 (blue), the purple group, and the green group. (d) The PM vector plot with colors and symbols the same as in panel (a) for member candidates.

2.3. Member Cleaning via the CMD

We construct a CMD for the 653 candidate stars of the four groups in Figure 2(a). The stars in the four groups surprisingly track a clear locus of a main sequence together, which is consistent with the PARSEC isochrone of 25 Myr with the sensitivity curves provided by Weiler (2018; black solid curve), adopting a reddening $E(B-V) = 0.07$ mag (Lyra et al. 2006) and a solar metallicity. Based on the nice fit of the isochrone to the data, the adopted age is in agreement with Currie et al. (2008), who obtained the age of NGC 2232 using ROSAT X-ray members. Different groups being coeval implies a common origin (see discussion in Section 3). Although NGC 2232 is suggested to be a metal-rich open cluster with a metallicity of $[\mathrm{Fe/H}] = 0.32 \pm 0.08$ (Monroe & Pilachowski 2010), the isochrone with a supersolar abundance (dotted curve in Figure 2(a)) is clearly shifted from the main-sequence locus toward redder colors due to the higher metallicity. Note that Monroe & Pilachowski's (2010) measurement was based on spectroscopic observations of four pre-main-sequence stars, whose lithium abundance is higher than that of the main-sequence stars due to lower effective temperatures (Juarez et al. 2014).

A dozen candidate stars are located below the main-sequence locus ($M_G > 4.7$ mag), corresponding to an age equal to or older than 100 Myr (gray dashed curve in Figure 2(a)). These stars are located on the outskirts of NGC 2232 and LP 2439. The RV of one star among these is four times larger than that of the other member candidates. Therefore, these are probably field stars. We use the 100 Myr isochrone as a reference and redden it to exclude possible contaminants. Around $M_G = 8$ mag is the transition region between pre-main-sequence stars and main-sequence stars. We redden the 100 Myr isochrone by 0.04 mag for magnitudes brighter than $M_G = 8$ mag and 0.1 mag for those with $M_G > 8$ mag. Stars bluer than the reddened isochrone are excluded from further analysis (black crosses in Figure 2(a)). After the CMD cleaning, 621 stars are selected as member candidates: 177 for NGC 2232 (blue), 315 for LP 2439 (red), 71 for purple, and 58 for green.

3. Properties of Identified Groups

3.1. Crossmatch with Previous Catalogs

Several new catalogs have recently been published for identifying new stellar groups with the multidimensional parameters from Gaia DR2. Recent work by Liu & Pang (2019) has identified star clusters in Gaia DR2 using the friends-of-friends (FoF) cluster finder in the 5D parameter space (l, b, ϖ, $\mu_\alpha \cos\delta$, and μ_δ). One of the 76 new clusters they discovered is LP 2439 (the red group). Among their 148 members for LP 2439, we recover 129 (orange circles in Figure 2(b)) in the present study. In addition, among the 177 member candidates that we identify in NGC 2232, 91 are crossmatched with the membership list of LP 2393 in Liu & Pang (2019; ID: 2393). As can be seen in Figure 2(b), members identified with the FoF cluster finder are all concentrated near the centers of the two clusters. Cantat-Gaudin et al. (2018) developed an unsupervised membership assignment code, UPMASK, to identify star clusters. In Cantat-Gaudin et al.'s (2018) study, 151 of the member candidates in NGC 2232 (blue) and six of the member candidates in the purple group (black circles in Figure 2(b)) are identified as members of NGC 2232 in Cantat-Gaudin et al. (2018).

Kounkel & Covey (2019) applied an unsupervised machine-learning technique and identified 1900 star clusters and strings in the Galactic disk. The strings that they identified are comoving groups with filamentary structures reaching up to ∼200 pc in length. They identified 328 strings with ages younger than 100 Myr in the solar neighborhood. Kounkel & Covey (2019) classified NGC 2232 as a string spanning 40° in the sky. The membership list of this NGC 2232 string in Kounkel & Covey (2019) crossmatches with 236 member candidates in LP 2439, 142 in NGC 2232, 32 in the purple group, and 30 in the green group (black plus signs in Figure 2(b)). Stars in strings are not only kinematically and spatially coherent but also coeval. Kounkel & Covey (2019) suggested that the extended shapes of the strings are primordial structures that originated from giant molecular filaments (Zucker et al. 2018).

Unlike Kounkel & Covey's (2019) claim of a "lack of a central cluster" among strings, NGC 2232 and LP 2439 not only stand out as two central clusters with significant overdensities in the space but also show two distinct overdensities in the PM distribution (Figure 2(d)). Their RV distributions slightly offset each other (Figure 2(c)), with average RVs of 22.0 and 25.4 km s^{-1} for LP 2439 and NGC 2232, respectively. The mean RV value obtained from Gaia DR2 for NGC 2232 agrees well with the mean RV of 25.40 km s^{-1} that was measured by Jackson et al. (2020) using the Gaia-ESO Survey. Considering the coevality of the four groups, they were likely formed during the same star formation event in the same GMC. Two local high-density regions in the GMC formed clusters, NGC 2232 and LP 2439. The purple and green groups consist of stars formed along the primordial filaments associated with NGC 2232, since their PM distributions are similar to NGC 2232, instead of LP 2439 (Figure 2(b)).

There is one member candidate in LP 2439 with a negative RV, −9.73 km s^{-1} (gray shaded bin in Figure 2(c)), different from the majority in LP 2439. Considering its location along the binary sequence (red outlined gray shaded star in Figure 2(a)), we conclude that it is a probable binary candidate. The other five member candidates with RV measurements are also binary candidates, being located along the binary sequence (filled stars in Figure 2(a)). Further follow-up spectroscopy may further constrain the nature of these stars.

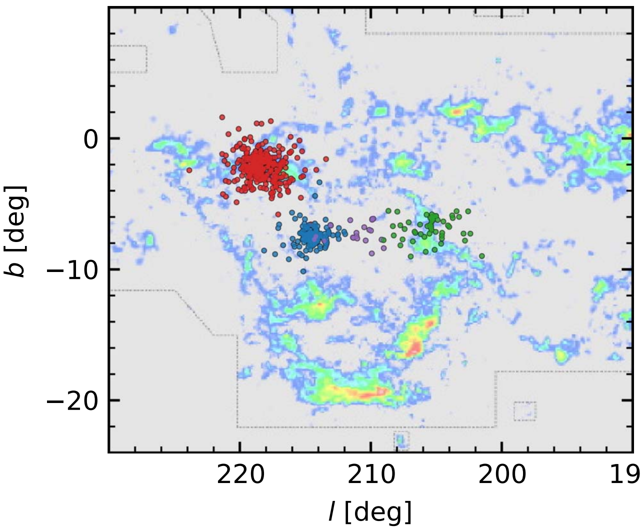

Figure 3. The CO emission map obtained from Dame et al. (2001) in the region where member candidates reside. The red dots are candidate members of LP 2439, and the blue dots are candidate members of NGC 2232. The purple and green dots represent the purple and green groups, respectively.

3.2. Evidence of Gas Expulsion

As indicated by the low reddening in NGC 2232 (Lyra et al. 2006), the gas content is very low in the region occupied by our member candidates. We overplot member candidates on the map of a large-scale CO survey of the Galactic plane (Dame et al. 2001; Figure 3). Toward the south of NGC 2232 are remarkably long and thin molecular filaments at $200° \lesssim l \lesssim 220°$ and $-20° \lesssim b \lesssim -10°$ that belong to the Orion cloud in the background (No. 27 in Table 1 in Dame et al. 2001; Figure 3) located at a distance of 414–437 pc (Hirota et al. 2007; Menten et al. 2007). It happens that LP 2439 overlaps with the CO emission at $-3° \lesssim b \lesssim 0°$ (No. 31 in Table 1 in Dame et al. 2001; Figure 3), which is induced by molecular clouds at a distance of 12–18 kpc from the Galactic center (May et al. 1993). The Leiden–Dwingeloo 21 cm survey (Hartmann & Burton 1997) also shows a very low column density of atomic hydrogen in the region of $200° \lesssim l \lesssim 220°$ and $-10° \lesssim b \lesssim 0°$. Therefore, the region at the distance of LP 2439, NGC 2232, and its related filamentary structures (the purple and green groups) can be considered free of gas and dust. This is direct evidence that the parental molecular gas from which the stars in NGC 2232 and LP 2439 were born has already been expelled by supernovae and/or stellar winds. The two clusters enter a phase of violent relaxation after gas expulsion (see discussion in Section 5).

4. 3D Morphology of NGC 2232 and LP 2439

4.1. Distance Correction

In panels (a)–(c) of Figure 4, we show the 3D spatial distributions of member candidates in NGC 2232, LP 2439, the purple group, and the green group. The shapes of these four groups are all stretched along the same direction: the line of sight (indicated with the black dashed lines). A similar

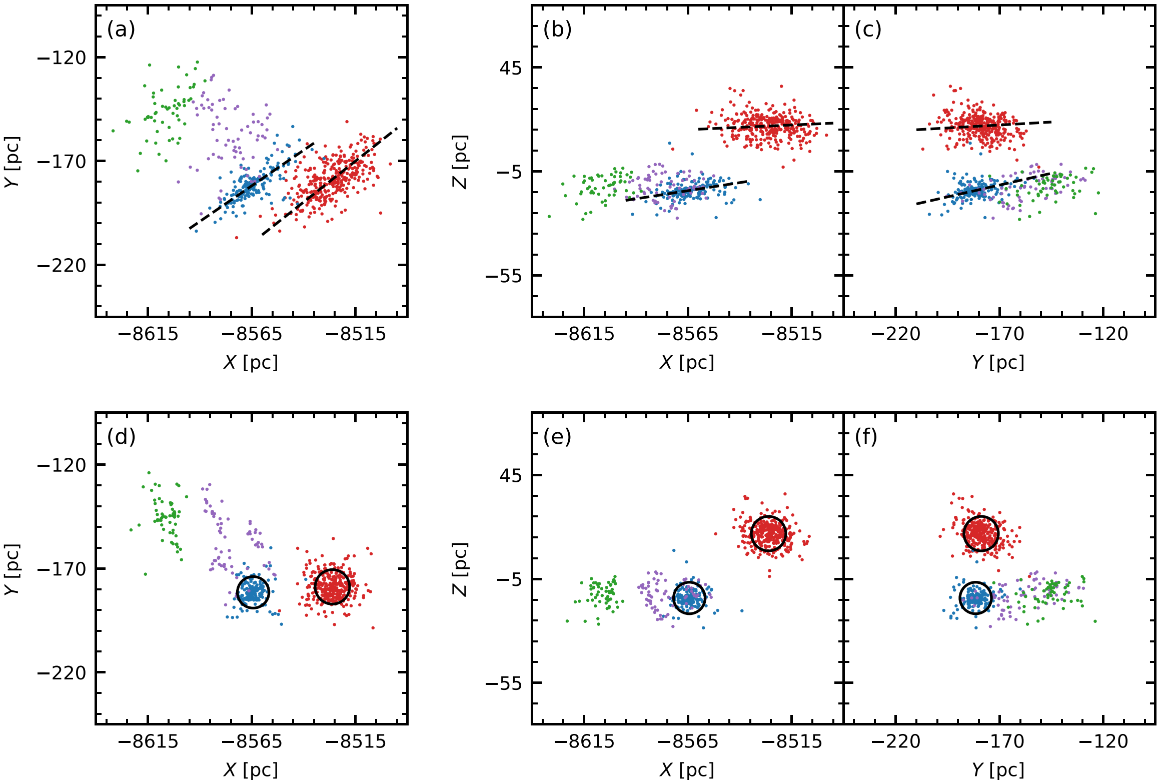

Figure 4. The 3D spatial position of member candidates in galactocentric Cartesian *X*, *Y*, *Z* coordinates. The colored symbols are the same as in Figure 2(a). Panels (a)–(c) display the positions before distance correction. The black dashed lines indicate the direction of the line of sight. Panels (d)–(f) show the 3D positions after distance correction via a Bayesian approach (see Section 4.1).

phenomenon was observed in another star cluster, Blanco 1 (Zhang et al. 2020). This artificial elongation is generated by the distance computed by simply inverting the parallax, $1/\varpi$. The errors in the parallax measurements $\Delta\varpi$ have a symmetric distribution function. After this reciprocation, the distance distribution becomes asymmetric. Member candidates in NGC 2232 and LP 2439 have ϖ in the range 2.92–3.87 and 2.78–3.46 mas, respectively. In an earlier study, we performed Monte Carlo simulations to estimate the contribution of the error $\Delta\varpi$ on the uncertainty in the evaluation of the *X*, *Y*, and *Z* coordinates (Zhang et al. 2020). A typical $\Delta\varpi$ of 0.19 mas (with a distance in the range 289–360 pc) corresponds to an error of 16–25 pc for our sample.

To correct for the pseudoelongation generated by parallax errors, we follow the Bayesian inversion approach introduced by Bailer-Jones (2015). We compute the likelihood based on the measured parallax combined with its nominal error with a prior designed for star clusters and field stars. The prior assumes a Gaussian spatial distribution of the star cluster members and an exponentially decreasing volume density for field stars (Bailer-Jones 2015). We adopt the standard deviation of the clustercentric distance of individual stars as the scale radius of the Gaussian distribution. For each star, the field and the cluster prior are combined with weights proportional to the estimated membership probability, which we assume is 95%, considering a 5% field star contamination rate (see Section 2.2). The corrected distance to each star is the mean value of the posterior distribution. A similar method has been applied to the star cluster M67 (Carrera et al. 2019, Appendix B); we refer to the latter work for further details on the method.

4.2. Interpretation of the 3D Morphology

After having corrected the distance measurements obtained from the Bayesian method, we display the projection of member candidates onto the *X*–*Y*, *X*–*Z*, and *Y*–*Z* planes (Figure 4, panels (d)–(f)). The intrinsic shapes of NGC 2232 and LP 2439 are more or less spherical, while the purple and green groups resemble filamentary structures stretching out to distances up to 50 pc. Their association with NGC 2232 is further confirmed by the proximity in the spatial distribution. Similar filamentary structures have been found in previous studies. Jerabkova et al. (2019) discovered the Orion relic filament, which extends 90 pc in space and is coeval, at an age of 17 Myr. Additional 250 pc long filamentary structures with ages in the range of 10–50 Myr were identified in the Vela OB2 region by Beccari et al. (2020). When assuming a prompt residual gas expulsion in a cluster with a star formation efficiency (SFE) of 1/3, a significantly elongated morphology will start to appear when star clusters are 80 Myr old (Dinnbier & Kroupa 2020b). Galactic tides need at least 100 Myr to develop two symmetric tidal tails in star clusters (Dinnbier & Kroupa 2020a). Therefore, the extended structures in both Orion and Vela OB2 are not tidal tails. This scenario is consistent with the observations that open clusters discovered with tidal tails have ages of at least 100 Myr (see Röser et al. 2019; Tang et al. 2019; Zhang et al. 2020).

According to the numerical study of Dinnbier & Kroupa (2020b), a star cluster with an SFE of 1/3 and a phase of rapid gas expulsion (model C10G13) will have about 50% unbound members (i.e., outside the tidal radius) at an age of 25 Myr. To test this scenario, we compute the tidal radii of NGC 2232 and

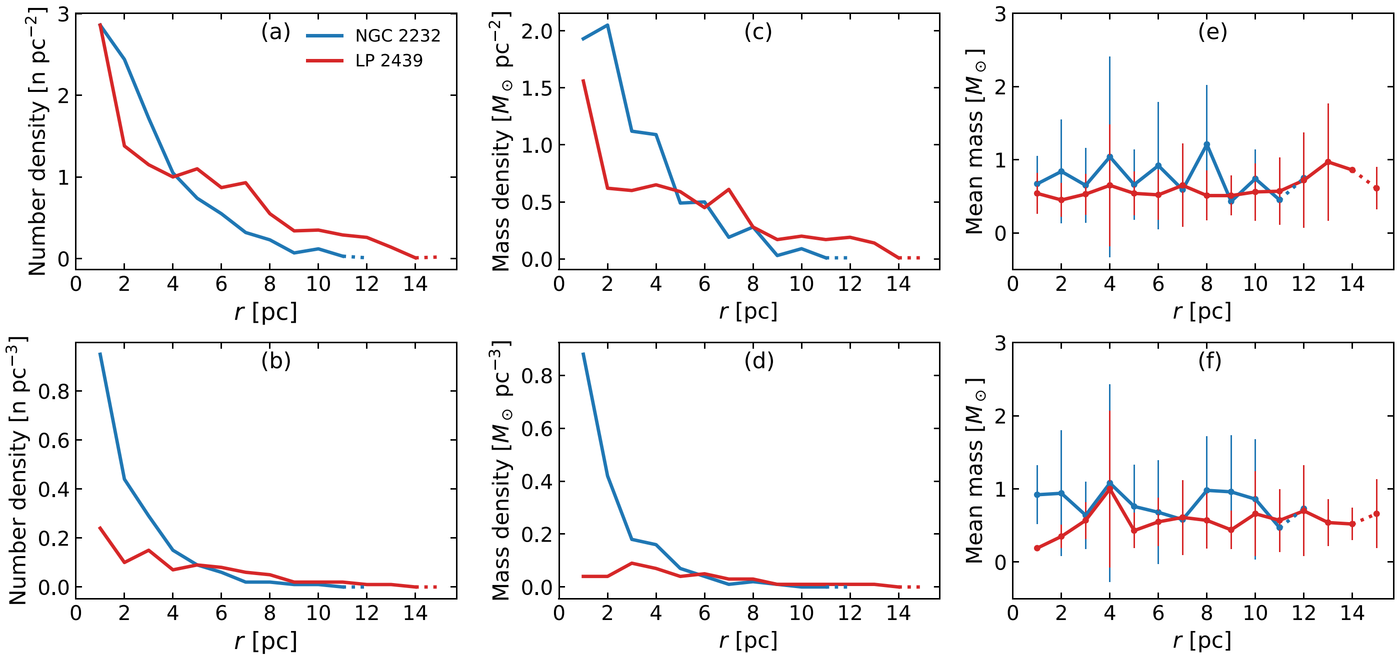

Figure 5. Number density, mass density, and mean mass distributions along a clustercentric distance r for NGC 2232 (blue curves) and LP 2439 (red curves). (a) Surface number density profile, (b) volume number density profile, (c) surface mass density profile, (d) volume mass density profile, (e) distribution of mean stellar mass in each surface annulus, (f) distribution of mean stellar mass in each volume annulus. The error bar is the standard deviation of the stellar mass in each annulus. The values for the outermost data points (at $r = 12$ pc for NGC 2232 and $r = 15$ pc for LP 2439) are computed using all cluster members with $r > 11$ pc (NGC 2232) and $r > 14$ pc (LP 2439).

LP 2439:

$$r_t = \left(\frac{GM_C}{2(A - B)^2}\right)^{\frac{1}{3}} \quad (1)$$

(Pinfield et al. 1998). Here G is the gravitational constant, M_C is the total mass of the star cluster, and the parameters A and B are the Oort constants ($A = 15.3 \pm 0.4$, $B = -11.9 \pm 0.4$ km s^{-1} kpc^{-1}; Bovy 2017).

From the photometric masses of 185.3 ± 17.7 and $140.5 \pm 9.4\,M_\odot$, obtained using a 25 Myr isochrone, we compute tidal radii of 8.3 ± 0.3 and 7.6 ± 0.2 pc for LP 2439 and NGC 2232, respectively. Errors are estimated from the 25 Myr isochrone with supersolar abundance (black dotted curve in Figure 2(a)). We assume that stars within the tidal radius are gravitationally bound to the star cluster, while those beyond the tidal radius are unbound. The tidal radius of LP 2439 is smaller than its half-mass radius of 8.8 pc, implying that more than half of the mass of the stellar grouping is gravitationally unbound. Note that the model cluster (model C10G13) in Dinnbier & Kroupa (2020b) is 10 times more massive than LP 2439; therefore, the required SFE should be higher to match the observed bound mass fraction in LP 2439 (48%). This implies that the scenario of an SFE higher than 1/3 and prompt gas expulsion may provide a good explanation of the observed properties of LP 2439.

On the other hand, NGC 2232 has a half-mass radius of 4.9 pc. Approximately 73% of its mass is gravitationally bound (i.e., within the tidal radius). For both LP 2439 and NGC 2232, we observe no tidal tails beyond the tidal radius. Instead, stars outside the tidal radius are more or less spherically distributed with respect to the cluster center.

To further quantify the spatial distribution of the stars, we plot the radial distribution of the number density, mass density, and mean stellar mass within different annuli of the two star clusters in Figure 5. The surface number density profiles and surface mass density profiles are similar for both clusters, with higher values in the center and a decline toward larger radius (Figures 5(a) and (c)). The volume number density profile and volume mass density profile in NGC 2232 share similar trends with its surface number density profile and surface mass density profile (Figures 5(b) and (d)). However, the case is quite different in LP 2439, where the volume number density profile and volume mass density profile are both very shallow (almost flat); see Figures 5(b) and (d). The members in LP 2439 are larger in number (315) than in NGC 2232 (177) and have a more extended spatial distribution (up to 32 pc) than NGC 2232 (up to 27 pc). The difference in surface and volume properties for LP 2439 originates in the projection effect of members located in larger 3D annuli onto 2D annuli.

The volume mass densities of both NGC 2232 and LP 2439 are comparable to those of a "leaky cluster" (mass-loss cluster), as defined in Pfalzner (2009). A mass-loss cluster is undergoing mass loss through a range of processes (gas expulsion, stellar and dynamical evolution, and tidal field) and expands at a velocity of 2 pc Myr^{-1} at early times. The expansion is probably more significant in LP 2439, since its volume mass density is approaching the lower limit of the observed "leaky clusters" of 0.07 $M_\odot$ pc^{-3} (Pfalzner 2009). All identified members are brighter than the Gaia DR2 photometric limit; deeper observations are therefore required to probe the contribution of faint members to the density profiles.

An inspection of the 2D and 3D spatial distribution of the member stars reveals no evidence of mass segregation in NGC 2232 and LP 2439 (see Figures 5(e) and (f)). On the other hand, stars enclosed within the 3–4 pc annulus are generally more massive and have a somewhat larger dispersion.

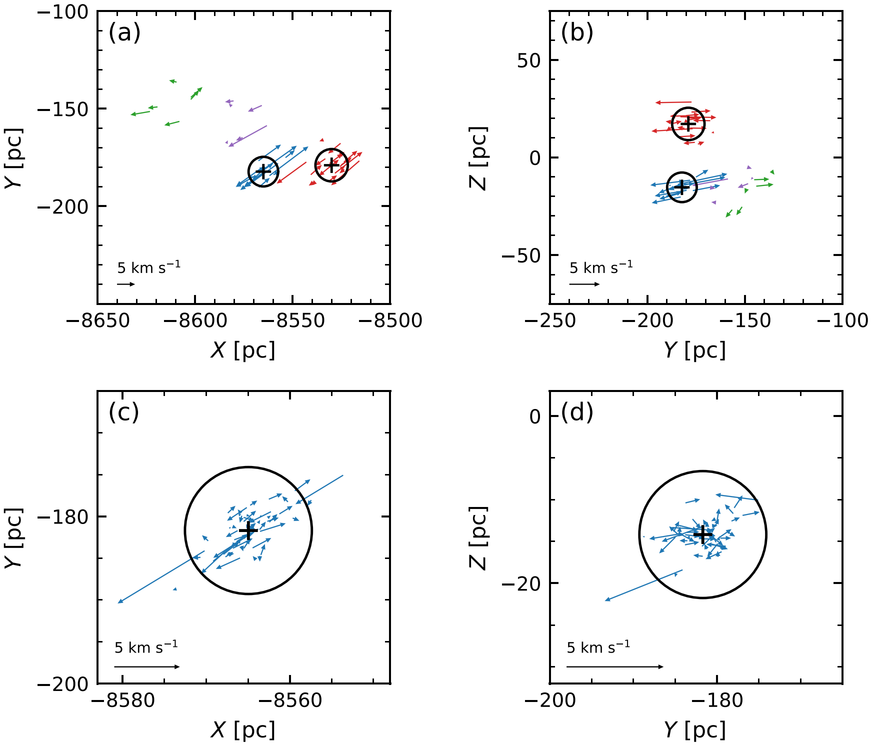

Figure 6. Relative 3D velocity vectors for member candidates projected onto *X*–*Y* and *Y*–*Z* planes. The red vectors represent the velocities of member candidates of LP 2439 relative to its mean motion, $(U, V, W) = (-8.3, 219.1, -4.0)$ km s^{-1}, and the blue vectors represent the velocities of member candidates of NGC 2232 relative to its mean motion, $(U, V, W) = (-9.3, 219.2, -3.7)$ km s^{-1}, as shown in panels (a) and (b). The RVs in panels (a) and (b) are obtained from Gaia DR2. The center of each cluster is indicated with a plus sign. Black circles denote the tidal radii. The purple and green vectors are the relative velocities of member candidates of the purple and green groups relative to the mean motion of NGC 2232. In panels (c) and (d), the blue vectors represent the relative velocities of members in NGC 2232 that are crossmatched with members in Jackson et al. (2020), with a membership probability larger than 90% relative to its mean motion, $(U, V, W) = (-9.7, 218.9, -3.8)$ km s^{-1}. The RVs in panels (c) and (d) are taken from Jackson et al. (2020). The scale of the velocity vectors is indicated in the bottom left corner of each panel.

5. Discussion

5.1. Expansion of LP 2439 and NGC 2232

We investigate the expansion of LP 2439 and NGC 2232 using the 3D motions of the member stars (through combining PMs and RVs). Only 20 members in LP 2439 and 17 in NGC 2232 have RV measurements. We use the mean positions of the member candidates in each cluster as the respective cluster centers of LP 2439 and NGC 2232 and the mean velocity in each cluster as the reference frame, and we present the relative 3D velocity in Figures 6(a) and (b). For this analysis, we consider the purple and green groups associated with NGC 2232 and use the mean motion of NGC 2232 as the reference velocity for these groups.

It can be clearly seen that both clusters are expanding, as their members are moving away from the cluster center (Figures 6(a) and (b)). However, the 3D velocity appears to be oriented primarily along the direction of the line of sight (see Figure 4). This can be explained by the orientation of the velocity error ellipsoid, of which the long axis is aligned with the line of sight. The typical error (median value) of the Gaia DR2 RV in our sample is 5.7 km s^{-1}, while the typical error of the PM is 0.25 km s^{-1}. Therefore, the error of the 3D velocity is dominated by the RV error, and the 3D velocity ellipsoid is elongated along the line of sight. To reduce this effect, we include the RV data of NGC 2232 from Jackson et al. (2020), who observed NGC 2232 using the Gaia-ESO Survey with an RV uncertainty of 0.4 km s^{-1}. Among the members with a membership probability larger than 90%, 51 members in Jackson et al. (2020; blue vectors) crossmatch with our members, which demonstrates the expansion within the tidal radius in NGC 2232 (see Figures 6(c) and (d)). A similar expansion is found in the intermediate-age cluster Coma Berenices for stars both within the tidal radius and located in the tidal tails (Tang et al. 2019). Since LP 2439 is a newly discovered star cluster, no high-resolution spectroscopic observations of its member stars are available as of yet.

The cluster expansion is initially spherically symmetric until the gradient of the Galactic gravitational potential deflects the stellar orbits (Kroupa 2005) and forms tidal tail–like structures. The spherical shapes of NGC 2232 and LP 2439 suggest that the Galactic tide has just started to affect the most distant candidates and has not yet affected the global morphology of the star clusters. While the majority of stars are moving outward, several members in both NGC 2232 and LP 2439 are falling back to the cluster, which may be a consequence of orbital epicyclic motions (Boily & Kroupa 2003; Dinnbier & Kroupa 2020a, 2020b).

For a 25 Myr old star cluster to spread over a region of 20 pc in size, an expansion velocity of at least 0.8 km s^{-1} is required. The measured 3D velocity dispersion may be overestimated due to orbital motion in binary systems (e.g., Kouwenhoven & de Grijs 2008). Since the latter affects RV measurements but not PMs, we compute the 2D velocity dispersion from PMs and obtain dispersions of 0.84 km s^{-1} for LP 2439 and 0.62 km s^{-1} for NGC 2232, with a typical error of 0.25 km s^{-1}. Considering the above calculation of velocity dispersion, the loose spatial distributions in both clusters can be explained well by the expansion that started approximately 20–25 Myr ago.

In addition to gas expulsion, two-body relaxation is another driver of expansion of the systems. This dynamical process drives massive stars to gradually sink to the cluster center and lower-mass stars to migrate to the outskirts. However, the radial distribution of the mean stellar mass within different annuli does not show evidence of mass segregation (see Figures 5(e) and (f)). Therefore, we propose that the expansion in both LP 2439 and NGC 2232 is mainly driven by gas expulsion that has taken place on a timescale shorter than the initial timescale of mass segregation.

The gas expulsion effect often induces a gradient of velocity dispersion (Kroupa 2005). The 2D velocity dispersion obtained from PMs does show a gradually increasing trend from the inner region toward the outskirts of the clusters. The 2D velocity dispersion starts at $\sigma_{\rm PM} = 0.71$ km s^{-1} within the tidal radius, increases to $\sigma_{\rm PM} = 0.94$ km s^{-1} outside the tidal radius for LP 2439, and increases from $\sigma_{\rm PM} = 0.56$ to 0.72 km s^{-1} for NGC 2232. These results are consistent with the predictions of Parmentier & Baumgardt (2012) and Dinnbier & Kroupa (2020a) that an expanding population of stars driven by gas expulsion has a larger velocity dispersion than that of the population within the tidal radius of the cluster, since escaping stars generally have "hotter" kinematics than the population of gravitationally bound stars.

5.2. Different Fates of NGC 2232 and LP 2439

After gas expulsion, NGC 2232 and LP 2439 enter a phase of violent relaxation. Whether or not they can manage to be virialized again depends on the duration of the revirialization process, which typically requires 20–40 crossing times (Parker & Wright 2016). To estimate how long it takes for a cluster to be revirialized, we compute the crossing time at the moment of gas expulsion by assuming an initial cluster radius of 1 pc and adopting the 2D velocity dispersion obtained from PM (see Section 5.1). The crossing times are estimated as $t_{\rm cr} \approx r_h/\sigma$, where r_h is the half-mass radius and σ is the 2D velocity dispersion obtained from PM (see Section 5.1). The crossing time of NGC 2232 is 1.6 Myr, and that of LP 2439 is 1.2 Myr. Note that, as the velocity dispersion at the onset of gas expulsion is likely higher, the estimated crossing times provide upper limits. The age of 25 Myr corresponds to at least $\sim 17\ t_{\rm cr}$ in NGC 2232 and 21 $t_{\rm cr}$ in LP 2439. Considering the 73% bound mass and the unremarkable density profile (Figure 5), NGC 2232 may be in the process of revirialization. On the other hand, with more than half of the mass unbound and a shallow volume density profile (Figure 5), LP 2439 is most likely in the process of dissolution.

Although NGC 2232 and LP 2439 originate from the same GMC, we witness two different dynamical fates, which stem from the different dynamical states right before the gas dispersal (Goodwin 2009; Farias et al. 2018). Assuming the same timescale of gas expulsion and the same SFE in NGC 2232 and LP 2439, we may conclude that NGC 2232 is initially subvirial and substructured, supported by the observed associated filamentary structures. On the contrary, LP 2439 may be in either a virial or supervirial state before the onset of gas expulsion. Since LP 2439 is more massive, the gas expulsion timescale may be much faster in LP 2439 than in NGC 2232, considering stronger stellar feedback from massive stars. The faster the gas expulsion, the faster the expansion of the cluster. Therefore, this results in a lower survival rate of clusters (Kroupa et al. 2001; Baumgardt & Kroupa 2007; Dinnbier & Kroupa 2020b). Either scenario supports the dissolution of LP 2439. Bravi et al. (2018) measured the RVs of three open clusters, IC 2602, IC 2391, and NGC 2547, in the age between 30 and 50 Myr and found that they are also expanding and dispersing. High-resolution spectroscopic data can be used to further constrain the dynamical history and fate of additional young star clusters in the Galactic field.

6. Summary

Utilizing high-precision Gaia DR2 astrometry, we apply the cluster-finding method, StarGO, to identify stellar structures around NGC 2232, LP 2439, and their neighboring regions in the 5D phase space of stars (X, Y, Z, $\mu_\alpha \cos\delta$, μ_δ). Additional member cleaning is carried out using the location of the candidate members in the CMD. The cluster LP 2439 was newly discovered by Liu & Pang (2019), and in this study, we quantify for the first time its dynamical state. Both clusters had their individual distance of member candidates corrected by a Bayesian method to further discuss their 3D morphology.

1. We have identified four groupings of stars in the sample: the clusters NGC 2232 and LP 2439 and two neighboring filamentary structures related to NGC 2232. The identification of the member candidates of the two star clusters is in good agreement with earlier studies. The ages of the four groups are consistent with an age of 25 Myr. This suggests that they all formed from the same GMC.
2. The member stars in LP 2439 have an average distance of 289.1 pc, with the center at R.A. = $103^\circ\!.3785$, decl. = $-05^\circ\!.8008$, corresponding to Cartesian galactocentric coordinates of $(X, Y, Z) = (-8526.5, -179.1, +16.8)$ pc. The tidal radius (8.3 pc) of LP 2439 is smaller than its half-mass radius (8.8 pc). More than half of the mass in this cluster is gravitationally unbound.
3. Member stars in NGC 2232 have an average distance of 323.0 pc, with the center at R.A. = $96^\circ\!.8931$, decl. = $-04^\circ\!.7697$, corresponding to Cartesian galactocentric coordinates $(X, Y, Z) = (-8564.0, -181.3, -14.2)$ pc. The tidal radius (7.6 pc) of NGC 2232 is larger than its half-mass radius (4.9 pc). More than 70% of the cluster's mass is gravitationally bound. We identify two filamentary structures (which we refer to as the purple group and the green group) that are associated with NGC 2232.
4. We observe no evidence of mass segregation among member candidates of LP 2439 and NGC 2232. We find an overall expansion in both star clusters that is mainly driven by gas expulsion. The expansion generates a loose and roughly spherically symmetric spatial distribution of stars. We observe a shallow volume number density profile and volume mass density profile for LP 2439.
5. Although NGC 2232 and LP 2439 are formed in the same GMC, our analysis suggests that these two star clusters will have different dynamical futures. While LP 2439 is undergoing violent dissolution, NGC 2232 may be in the process of revirialization. We propose that this reflects different initial dynamical states prior to gas expulsion in the two clusters. We propose two possibilities to explain how these star clusters ended up in their current states: (i) prior to gas removal, NGC 2232 may have been substructured and subvirial, while at the same time, LP 2439 may have been either in virial equilibrium or

supervirial; or (ii) gas expulsion in LP 2439 occurred at a much faster rate than in NGC 2232.

X.Y.P. is grateful for the financial support of two grants from the National Natural Science Foundation of China, Nos. 11503015 and 11673032. This study is supported by the development fund of Xi'an Jiaotong Liverpool University (RDF-18–02–32). M.B.N.K. expresses gratitude to the National Natural Science Foundation of China (grant No. 11573004) and the Research Development Fund (grant RDF-16–01–16) of Xi'an Jiaotong Liverpool University (XJTLU). M.P. acknowledges financial support from the European Union's Horizon 2020 research and innovation program under Marie Sklodowska-Curie grant agreement No. 664931.

We are grateful to the referee for providing in-depth comments and suggestions that greatly helped to improve this paper. We send our gratitude to Prof. Dr. Pavel Kroupa and Dr. Frantisek Dinnbier for detailed discussion of the dynamical evolution of star clusters. We express thanks to Prof. Dr. Yu Gao and Hongjun Ma for helpful suggestions on CO emission.

This work made use of data from the European Space Agency (ESA) mission Gaia (https://www.cosmos.esa.int/gaia), processed by the Gaia Data Processing and Analysis Consortium (DPAC; https://www.cosmos.esa.int/web/gaia/dpac/consortium). This study also made use of the SIMBAD database and the VizieR catalog access tool, both operated at CDS, Strasbourg, France.

Software: `Astropy` (Astropy Collaboration et al. 2013, 2018), `SciPy` (Millman & Aivazis 2011), `TOPCAT` (Taylor 2005), and StarGO (Yuan et al. 2018).

ORCID iDs

Xiaoying Pang https://orcid.org/0000-0003-3389-2263
Shih-Yun Tang https://orcid.org/0000-0003-4247-1401
M. B. N. Kouwenhoven https://orcid.org/0000-0002-1805-0570

References

Adams, F. C. 2000, ApJ, 542, 964
Astropy Collaboration, Price-Whelan, A. M., Sipőcz, B. M., et al. 2018, AJ, 156, 123
Astropy Collaboration, Robitaille, T. P., Tollerud, E. J., et al. 2013, A&A, 558, A33
Bailer-Jones, C. A. L. 2015, PASP, 127, 994
Banerjee, S., & Kroupa, P. 2013, ApJ, 764, 29
Baumgardt, H., & Kroupa, P. 2007, MNRAS, 380, 1589
Beccari, G., Boffin, H. M. J., & Jerabkova, T. 2020, MNRAS, 491, 2205
Boily, C. M., & Kroupa, P. 2003, MNRAS, 338, 665
Bovy, J. 2017, MNRAS, 468, L63
Bravi, L., Zari, E., Sacco, G. G., et al. 2018, A&A, 615, A37
Brinkmann, N., Banerjee, S., Motwani, B., et al. 2017, A&A, 600, A49
Cantat-Gaudin, T., Jordi, C., Vallenari, A., et al. 2018, A&A, 618, A93
Carrera, R., Pasquato, M., Vallenari, A., et al. 2019, A&A, 627, A119
Claria, J. J. 1972, A&A, 19, 303
Cottaar, M., Meyer, M. R., Andersen, M., et al. 2012, A&A, 539, A5
Cropper, M., Katz, D., Sartoretti, P., et al. 2018, A&A, 616, A5
Currie, T., Plavchan, P., & Kenyon, S. J. 2008, ApJ, 688, 597
Dame, T. M., Hartmann, D., & Thaddeus, P. 2001, ApJ, 547, 792
de Grijs, R., & Goodwin, S. P. 2008, MNRAS, 383, 1000
Dinnbier, F., & Kroupa, P. 2020a, arXiv:2007.00036
Dinnbier, F., & Kroupa, P. 2020b, arXiv:2006.14087
Farias, J. P., Fellhauer, M., Smith, R., et al. 2018, MNRAS, 476, 5341
Farias, J. P., Smith, R., Fellhauer, M., et al. 2015, MNRAS, 450, 2451
Gaia Collaboration, Babusiaux, C., van Leeuwen, F., et al. 2018a, A&A, 616, A10
Gaia Collaboration, Brown, A. G. A., Vallenari, A., et al. 2018b, A&A, 616, A1
Goodwin, S. P. 2009, Ap&SS, 324, 259
Goodwin, S. P., & Bastian, N. 2006, MNRAS, 373, 752
Hartmann, D., & Burton, W. B. 1997, Atlas of Galactic Neutral Hydrogen (Cambridge: Cambridge Univ. Press)
Hills, J. G. 1980, ApJ, 235, 986
Hirota, T., Bushimata, T., Choi, Y. K., et al. 2007, PASJ, 59, 897
Jackson, R. J., Jeffries, R. D., Wright, N. J., et al. 2020, MNRAS, 496, 4701
Jerabkova, T., Boffin, H. M. J., Beccari, G., et al. 2019, MNRAS, 489, 4418
Juarez, A. J., Cargile, P. A., James, D. J., & Stassun, K. G. 2014, ApJ, 795, 143
Karnath, N., Prchlik, J. J., Gutermuth, R. A., et al. 2019, ApJ, 871, 46
Kounkel, M., & Covey, K. 2019, AJ, 158, 122
Kouwenhoven, M. B. N., & de Grijs, R. 2008, A&A, 480, 103
Kroupa, P. 2005, in Gaia Symp. Proc. ESA SP-576, The Three-dimensional Universe with Gaia, ed. C. Turon, K. S. O'Flaherty, & M. A. C. Perryman (Noordwijk: ESA), 629
Kroupa, P., Aarseth, S., & Hurley, J. 2001, MNRAS, 321, 699
Lada, C. J., & Lada, E. A. 2003, ARA&A, 41, 57
Levato, H., & Malaroda, S. 1974, AJ, 79, 890
Lindegren, L., Hernández, J., Bombrun, A., et al. 2018, A&A, 616, A2
Liu, L., & Pang, X. 2019, ApJS, 245, 32
Lynden-Bell, D. 1967, MNRAS, 136, 101
Lyra, W., Moitinho, A., van der Bliek, N. S., et al. 2006, A&A, 453, 101
May, J., Bronfman, L., Alvarez, H., et al. 1993, A&AS, 99, 105
Menten, K. M., Reid, M. J., Forbrich, J., et al. 2007, A&A, 474, 515
Millman, K. J., & Aivazis, M. 2011, CSE, 13, 9
Moeckel, N., Holland, C., Clarke, C. J., et al. 2012, MNRAS, 425, 450
Monroe, T. R., & Pilachowski, C. A. 2010, AJ, 140, 2109
Pang, X., Grebel, E. K., Allison, R. J., et al. 2013, ApJ, 764, 73
Pang, X., Pasquali, A., & Grebel, E. K. 2011, AJ, 142, 132
Pang, X., Shen, S., & Shao, Z. 2018, ApJL, 868, L9
Parker, R. J., & Wright, N. J. 2016, MNRAS, 457, 3430
Parmentier, G., & Baumgardt, H. 2012, MNRAS, 427, 1940
Parmentier, G., & Pfalzner, S. 2013, A&A, 549, A132
Pfalzner, S. 2009, A&A, 498, L37
Pinfield, D. J., Jameson, R. F., & Hodgkin, S. T. 1998, MNRAS, 299, 955
Röser, S., Schilbach, E., & Goldman, B. 2019, A&A, 621, L2
Rybizki, J., Demleitner, M., Fouesneau, M., et al. 2018, PASP, 130, 74101
Scandariato, G., Robberto, M., Pagano, I., et al. 2011, A&A, 533, A38
Shukirgaliyev, B., Parmentier, G., Berczik, P., et al. 2017, A&A, 605, A119
Tang, S.-Y., Pang, X., Yuan, Z., et al. 2019, ApJ, 877, 12
Taylor, M. B. 2005, in ASP Conf. Ser. 347, Astronomical Data Analysis Software and Systems XIV, ed. P. Shopbell, M. Britton, & R. Ebert (San Francisco, CA: ASP), 29
Weiler, M. 2018, A&A, 617, A138
Yuan, Z., Chang, J., Banerjee, P., et al. 2018, ApJ, 863, 26
Zhang, Y., Tang, S.-Y., Chen, W. P., et al. 2020, ApJ, 889, 99
Zucker, C., Battersby, C., & Goodman, A. 2018, ApJ, 864, 153